# Formation of Three-Dimensional Structures in the Hemisphere-Cylinder

S. Le Clainche*
*Universidad Politécnica de Madrid, 28040 Madrid, Spain*
D. Rodríguez†
*Universidade Federal Fluminense, 24220-900 Niterói - RJ, Brazil*
V. Theofilis‡
*University of Liverpool, Liverpool L69 3GH, United Kingdom*
and
J. Soria§
*Monash University, Clayton, Victoria 3800, Australia*

DOI: 10.2514/1.J055011

**This paper presents an investigation of the origin and evolution of the complex flow pattern on a hemisphere-cylinder at separated flow conditions. Three-dimensional numerical simulations have been performed for a range of Reynolds numbers and angles of attack. A critical point theory has been used to analyze the flowfields. This has yielded, for the first time for this geometry, a bifurcation diagram that classifies the different flow topology regimes as a function of the Reynolds number and angle of attack. A complete characterization of the origin and evolution of the complex structural patterns of this geometry is documented. For the higher Reynolds number and angle of attack, a structurally stable topology is found that is associated with the pattern of the horn vortices, usually found on this geometry in a range from low to high Reynolds numbers and from incompressible to compressible regimes. Surface critical points and surface and volume streamlines describe the main flow structures and their strong dependence with the flow conditions.**



## I. Introduction

FLOW separation over inclined axisymmetric bodies such as the hemisphere-cylinder (HC) is usually associated with problems of flight stability and control. Due to its numerous applications, such as in aircraft fuselages, missiles, and submarines, the study of the flow around the hemisphere-cylinder geometry, at both zero and nonzero angles of attack (AOAs), has been the subject of several experimental and computational investigations. The main goal has been to understand how flow separation affects aerodynamic properties: particularly, the forces and moments on the hemisphere-cylinder body.

The importance of the prediction and control of three-dimensional separation relies on the highly undesirable effects that it can cause on the aerodynamic characteristic and structural loads of the object. Massive flow separation leads to stall conditions on lifting bodies to the formation of large detached vortices, the interaction of these vortical patterns, and the subsequent destabilization downstream of control surfaces. In addition, separation increases local heat transfer on reattachment zones, causing problems in high-speed flights (e.g., the hypersonic "Columbia" Space Shuttle and the slender-wing supersonic "Concorde" transport aircraft) [1]. Low-Reynolds-number flow separation around the nose of the hemisphere-cylinder is a prototype case of essentially three-dimensional laminar flow separation. At certain flow conditions, depending on the Reynolds number $Re$, Mach number, and AOA, the qualitative physical picture emerging when massive flow separation occurs on a hemisphere-cylinder is a laminar separation bubble that, at high incidence of the body, results in a pair of counter-rotating vortices originated in the separation bubble, commonly referred to as "horn" vortices (HV). The unsteady nature of these vortices may generate unsteady structural loads affecting to the size and shape of the mean separated region, and consequently conditioning vehicle stability. In addition, the crossflow pressure gradient on the inclined circular cylinder causes the boundary layer to separate on the lee sides and roll up, generating the so-called "leeward" vortices (LV) (see figure in work by Hoang et al. [2]).

Motivated by the improvements in the capabilities of air-to-air missiles, intensive research was conducted in order to improve the existing predictive methods for their aerodynamic performance. The high AOA attained by these vehicles lead to massive three-dimensional separation; hence, the methods used traditionally in aircraft industry, mainly based on potential flow, were not adequate. It was then, when the flow topology laws (introduced and expanded successively by Legendre [3], Lighthill [4], Perry and Fairlie [5], Dallman [6], Tobak and Peake [7], and Perry and Chong [8]) became useful in the analysis of the flow structures in three-dimensional separated flows to enable the deduction of mean flow characteristics. These laws provided a theoretical foundation for the analysis and description of the flow patterns in situations where lack of resolution (both experimental and numerical) might cause inaccuracies in the study of these kindd of complex flows.

Hsieh [9–11] was the first to study the flow around a hemisphere-cylinder in low supersonic flow. The author was able to identify three different separation patterns as a function of the Reynolds number, Mach number, and AOA:

1) The first pattern is crossflow separation, resulting from the crossflow pressure gradient (i.e., a direct consequence of AOA) that causes a pair of leeside vortex sheets that wind over themselves forming the leeward vortices.

2) The second pattern is the nose separation bubble (SB), caused by the meridional pressure gradient.

3) The third pattern are the secondary separation lines defining the secondary leeward vortices that appear when the crossflow pressure gradient is intense enough.

Received 11 January 2016; revision received 25 May 2016; accepted for publication 22 June 2016; published online 31 August 2016. 

*School of Aeronautics; soledad.leclainche@upm.es (Corresponding Author).

†Graduate, Mechanical Engineering Department; also Pontifical Catholic University of Rio de Janeiro, 38097 Rio de Janeiro, Brazil.

‡School of Engineering, The Quadrangle, Brownlow Hill; also School of Aeronautics, Universidad Politécnica de Madrid, 28040 Madrid, Spain.

§Laboratory for Turbulence Research and Combustion; also Department of Aeronautical Engineering, King Abdulaziz University, Jeddah 21589, Saudi Arabia.

Next, Fairlie [12] studied prolate-spheroid and hemisphere-cylinder geometries in incompressible flow at $Re \simeq 1.5 \times 10^6$ and high AOAs. He found that, when the AOA was larger than 17.5 deg, the horn vortices emerged from the body surface: two spiral nodes, symmetrically located about the leeward plane of symmetry, gave rise to a pair of counter-rotating vortices that were shed downstream.

Further subsequent investigations were carried out to study the three-dimensional complex topology patterns developed above the body surface, based on critical point theory. Based on this theory, Tobak and Peake [7,13,14] were the first to identify and classify critical points and separation lines on the hemisphere-cylinder body surface in compressible flows. They pointed out the existence of two unstable foci, associated with the emergence of the horn vortices; a saddle and a node point; related to a separation bubble; as well as a reattachment line and primary and secondary lines of separation, related to the leeward vortices. Additionally, this study found that compressibility altered quantitatively the flow characteristics, but that the topological patterns on the surface of the hemisphere-cylinder were equivalent between compressible and incompressible regimes. Supplementary to this hypothesis, Bippes and Turk [15] studied the influence of the Mach number, Reynolds number, and AOA over the same geometry and found that the structural flow patterns in stable laminar flow were very similar to the ones found in turbulent separated flow.

A sequence of experiments performed in the early 1980s using surface hot-film sensors [16,17] and laser Doppler velocimetry [18,19] studied in more detail these leeward vortices (previously detected by Hsieh [9]), far from the body nose. It was postulated that the contribution of substantial crossflow and heavily inflectional profiles of the boundary layer on the leeside caused the development of vortex sheets that ultimately formed the counter-rotating leeward vortices, which were not able to remain laminar for large Reynolds number (transitioning to a turbulent regime). In addition, Hsieh and Wang [20] provided numerical evidence in support of this flow pattern.

Several authors continued the work and contributed with their research. Mead and Schiff [21] studied surface pressure distributions and their variations in the separation bubble region in supersonic flows. Ying et al. [22] suggested that the horn vortices might appear in an asymmetric fashion, but Hoang et al. [2,23], who studied experimentally the influence of the Reynolds number and AOA on these vortex pair in incompressible flows, did not find evidence of such asymmetry. In addition, these latter authors found that the nose structures and the separation lines, which gave rise to the vortical structures over the aft part of the body, were not connected.

More recently, Gross et al. [24] performed direct numerical simulations and experiments at moderate Reynolds numbers ($Re_D = 2000$ and $Re_D = 5000$) and moderate-to-high incidence. At AOA = 10 deg, they determined the presence of long separation bubble shedding structures that were primarily two-dimensional (2-D), suggesting that the dominant mechanism of such flow oscillations was an inviscid linear shear-layer instability on the symmetry plane. However, the geometry studied by these authors was different in the rear part of the body to the classic HC geometry studied in the literature mentioned previously. They studied the so-called DARPA suboff bare hull geometry, for which the rear part was extended smoothly to form a fuselaged tail. On the contrary, the HC body ended in a plane cylinder base, constituting a bluff body and then giving rise to a wide wake. As found by Gross et al. [24], flow oscillations in three-dimensional separated flows might be dominated by an inflectional instability and become unstable at relatively small Reynolds numbers [25]. However, the three-dimensional nature of the flow around a hemisphere-cylinder prevented, in principle, the use of traditional linear stability analysis based on one-dimensional velocity profiles. Methodologies for global instability analysis needed to be employed. On the other hand, large-scale coherent structures in turbulent flows were often reminiscent of flow structures generated by linear instabilities, especially in mixing layers flows (e.g., Crow and Champagne [26], Gaster et al. [27], Reynolds and Hussain [28], etc.).

Coming back to the HC, Bohorquez et al. [29] and Sanmiguel-Rojas et al. [30] performed numerical simulations at AOA = 0 deg, finding bifurcations of the linear global stability modes on the wake as a function of the Reynolds number and the aspect ratio ($\mathcal{AR}$) of the body (length/diameter). A global mode was found to be associated with the instability of the counter-rotating vortex pair forming the three-dimensional wake, with the associated nondimensional frequency of $St \simeq 0.11$. Similar frequencies were found by many authors that studied flows past bluff bodies [31,32]. This result was in good agreement with the standard weakly nonlinear theory for Hopf bifurcation [33]. Finally, Le Clainche et al. [34], who studied the HC at high AOAs and low Reynolds numbers, also found the same frequency related with the wake oscillations. These authors found that the onset of unsteadiness in the HC was due to an instability in the three-dimensional wake with a frequency of $St \simeq 0.11$. The fluctuations commenced close to the cylinder base and were convected downstream. This effect suggested that the base of the cylinder played a fundamental role in the primary instability of this flow. However, to totally understand this behavior, the mechanism of flow separation, and its connection with the horn vortices, it was necessary to study more in depth the origin and evolution of the complex structural patterns characterizing the geometry.

In the past, topology patterns have been analyzed over different configurations on a hemisphere-cylinder at high AOAs in compressible and incompressible regimes employing both experimental and numerical techniques at high Reynolds numbers. However, the origin of the complex topological patterns is still an open question. These patterns evolved from laminar regimes starting from very low values of Reynolds numbers until they achieved the more classical configuration presented in the literature [14].

This paper explains the origin and evolution of the critical points on the surface of a hemisphere-cylinder, and it details the analysis of three-dimensional topological patterns that precede the formation of the three well-known topology patterns found in this geometry: the separation bubble, the horn vortices, and the leeward vortices. For the first time, a bifurcation diagram that classifies the different flow topology regimes as functions of the Reynolds number and AOA is presented for this geometry.

The paper is organized as follows: Sec. II defines the geometry and the numerical code, and it demonstrates the convergence of the presented results. Section III reviews in detail the critical point theory. Section IV introduces and classifies the results in the bifurcation diagram. Section V shows the results. Finally, a brief discussion and the main conclusions are presented in Sec. VI.

## II. Model Description and Numerical Simulations

Three-dimensional numerical simulations are performed to study the flow around a hemisphere-cylinder with an aspect ratio of $\mathcal{AR} = L/D$, where $L$ and $D$ are the length and diameter of the body, respectively. In addition, the angle $\Phi$ is defined in the azimuthal direction and is measured positive in the clockwise direction. The value of this angle corresponds to zero on the symmetry plane of the body (see Fig. 1b).

Flow topology and structural analysis are carried out for several combinations of AOA and Reynolds number ($Re$), which is defined as $Re = U_\infty D/\nu$, where $U_\infty$ is the freestream velocity and $\nu$ represents the kinematic viscosity. Figure 1 shows the model and the parameters defined for the analysis. More details about the geometry can be found in the work by Le Clainche [35].

### A. Numerical Simulations

Three-dimensional numerical simulations are carried out for Reynolds numbers ranging from 100 to 1000 and AOAs from 0 to 30 deg in a HC geometry with $\mathcal{AR} = 8$. Table 1 summarizes the numerical simulations performed.

#### 1. Numerical Code

The numerical code used for the simulations is OpenFOAM 2.0, which is an open-source computational fluid dynamics software.[¶]

[¶]Data available online at http://www.openfoam.com [retrieved 2016].

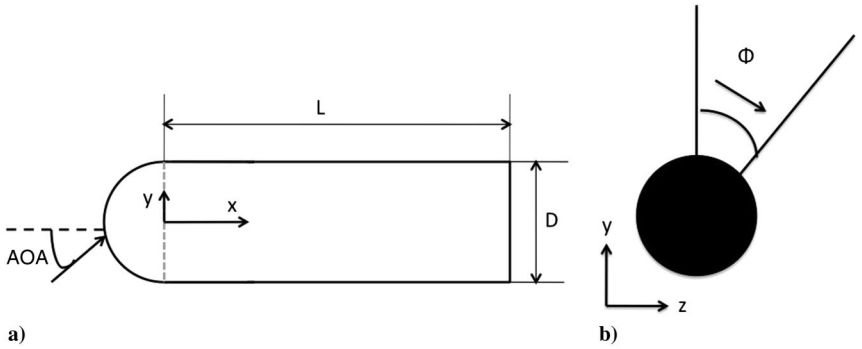


**Fig. 1 Representations of a) hemisphere-cylinder dimensions (side view) and b) azimuthal angle into the hemisphere-cylinder (front view).**



High-quality results over axisymmetric bodies related to linear stability analysis using this code have been recently reported [29,30,36,37].

The module employed in OpenFOAM discretizes the incompressible Navier–Stokes equations using a finite volume method. The spatial and temporal discretizations are performed using a central difference scheme (linear interpolation scheme to relate cell center and face center values) for both the convective and diffusive terms and a Crank–Nicholson scheme, respectively, with second-order accuracy in both cases (see work by Le Clainche [35] for further numerical details).

### 2. *Computational Domain and Boundary Conditions*

The computational domain is a coaxial cylindrical surface rotated 360 deg (fully three-dimensional) of diameter $20D$ and length $50D$. This length is demonstrated to be sufficient to accurately capture the physics of the problem in the case with AOA $= 0$ deg [29,30], and is therefore used for the present study. The mesh employed is generated using the OpenFOAM utility BlockMesh. It is composed of a regular tetrahedral grid. To avoid numerical singularities, the mesh within the sphere region is created following the numerical algorithm that defines a cubic sphere [38].

No-slip boundary conditions are employed on the body surface and freestream boundary conditions on the far field using $\boldsymbol{u}(\boldsymbol{x}, t) = (U_\infty \cos(\text{AOA}), U_\infty \sin(\text{AOA}), 0)$ in the inlet and sides of the domain (with $U_\infty = 1$) and $p(\boldsymbol{x}, t) = 0$ in the outlet.

### 3. *Study of Convergence and Validation*

A mesh containing $\sim 2.8 \times 10^6$ tetrahedral cells is used for the numerical simulations at $Re \geq 350$. Le Clainche et al. [39] showed that the frequency spectrum observed in the velocity field close to the nose region converges for the specific resolution and the numerical error is below 3% for drag coefficient calculations at $Re = 1000$ and AOA $= 20$ deg (the most demanding case considered in this analysis). Hsieh and Wang [20] showed that the flow topology patterns found in the hemisphere-cylinder were always present in the flow physics description of this geometry; thus, they could be considered as a robust physical phenomenon. The robustness of this flow pattern led to the identification of the critical points that define the laminar separation bubble, even in cases of limited spatial resolutions. Le Clainche et al. [40] identified the critical points defining the separation bubble at $Re = 1000$ and AOA $= 20$ deg using the same numerical code and a mesh containing $\sim 10^5$ cells. The small quantitative errors in the location of the critical points did not have the potential to modify the topological description of the flow, and they are considered to be acceptable for the present analysis.

**Table 1 Numerical simulations performed on the hemisphere-cylinder with $\mathcal{R} = 8$ (marked X)**

| | Reynolds number | | | | | | | | | |
|---|---|---|---|---|---|---|---|---|---|---|
| AOA | 100 | 150 | 200 | 250 | 300 | 350 | 400 | 450 | 500 | 1000 |
| 30 | — | — | — | — | — | — | — | — | — | X |
| 20 | X | X | X | X | X | X | X | X | X | X |
| 15 | — | X | X | X | X | X | X | — | — | X |
| 10 | — | — | X | — | X | — | X | — | — | X |
| 5 | — | — | — | X | — | — | — | X | — | X |
| 0 | — | — | — | — | — | — | — | — | — | X |

The numerical simulations have been validated with time-resolved particle image velocimetry experiments (presented in work by Le Clainche et al. [39]) and with the literature [29,37]. The drag coefficient of the HC with $\mathcal{R} = 2$ is compared with the results obtained by Sanmiguel-Rojas et al. [37] at $Re = 300$ and AOA $= 0$ deg. The relative error defined as $\varepsilon(\%) = |(C_D - C_{D0})/C_{D0}| \cdot 100$ (where $C_{D0}$ is the drag coefficient obtained from the literature, and $C_D$ is the drag coefficient obtained in the present simulations) is smaller than 2.5%. This is considered to be sufficiently small to carry out the structural analysis. The small differences between the present data and the previously published results are most likely due to the different numerical schemes employed in both cases. Sanmiguel-Rojas et al. [37] used a total variation-diminishing (TVD) scheme as spatial discretization to solve the numerical simulations. However, the present authors use a central differencing scheme: in particular, a linear interpolation scheme. TVD schemes are known to be highly dissipative, whereas central differencing schemes are associated with low numerical dissipation and high dispersion. Dissipative effects can reduce the effective Reynolds number, and they could explain the smaller values obtained for the drag coefficient in the present investigation compared to the values obtained in the literature. Nevertheless, this small error (~2.5%) is assumed to be admissible in the results presented herein.

## III. Critical Points Theory

Critical point theory is a technique that was introduced sequentially by Legendre [3], Lighthill [4], Perry and Fairlie [5], Dallman [6], Tobak and Peake [7], and Perry and Chong [8] to describe the topological features of flow patterns. A critical point is a location in space where the three components of the velocity vector are all simultaneously zero and the streamline slope is undetermined. Using Taylor series to expand the flow around the critical points, and only retaining the linear terms, the flow expansion can be represented via the Jacobian matrix $J$ as $\dot{\boldsymbol{x}} = J\boldsymbol{x}$, where $\boldsymbol{x}$ is the vector representing the spatial coordinates and $\dot{\boldsymbol{x}}$ represents its time derivatives.

The eigenvectors of the Jacobian matrix define the planes of the flow trajectories around the critical points, whereas the eigenvalues $\lambda$ of the Jacobian matrix satisfy the following equation:

$$\lambda^3 + P\lambda^2 + Q\lambda + R = 0 \tag{1}$$

where $P$, $Q$, and $R$ are defined as the trace, the discriminant, and the determinant of $J$, respectively.

In incompressible flows, the divergence of the velocity field is zero; so, in Eq. (1), $P = 0$ and the critical points are classified according to their location in the $Q$-$R$ plane: the $Q$-$R$ chart [41]. The curve solution $T = 27R^2 + 4Q^3$ separates real and complex eigenvalues.

Depending on the nature of the eigenvalues $\lambda$, critical points are classified as nodes ($Q > 0$, $T < 0$), foci ($Q > 0$, $T > 0$), saddle

points ($Q < 0$), and a sequence of borderline cases. Nodal and focal points can be either stable (sink of streamlines) or unstable (source of streamlines), depending on whether the streamlines are attracted toward or repelled from the critical point, respectively. Borderline cases are a mixture of two different critical points (i.e., $P = 0 \rightarrow$ node-saddle or $Q = 0 \rightarrow$ node-foci/starnode). On a body surface, since the velocity vector is equal to zero, the wall shear stress is used instead for the critical point calculations. Wall streamlines are then called skin-friction lines.

For a body totally immersed in a flow, a set of topological rules has been postulated in the literature [14]. One of these, which is of particular relevance to this work, stated that the number of nodes or foci minus the number of saddles on a three-dimensional body was equal to two [4,42]:

$$\sum N - \sum S = 2 \tag{2}$$

## IV. Topological Bifurcations and Phase Diagram

The results obtained from the numerical simulations for the hemisphere-cylinder with $\mathcal{AR} = 8$ are classified in a topological bifurcation diagram as a function of the Reynolds number and AOA. In the diagram, it is possible to identify steady–unsteady flow and attached–separated flow. Additional classifications are included, depending on the nature of the separation bubble. Figure 2a shows the phases diagram, in which six different regimes are identified for the first time in this work. The flow is steady in the two first regimes, whereas it is unsteady in the other regimes. The diagram also distinguishes two kind of separation topologies based on the type of point of separation that defines the separation bubble (node or saddle): the separation process is known as local (node) or global (saddle) [14]. The regimes are described as follows:

1) Regime I is steady attached flow.

2) Regime II is steady state with local nose separation. The separation bubble is described by a node of separation (local separation), a node of reattachment, and two saddles $S_I$ symmetrically positioned with respect to the symmetry plane.

3) Regime III is unsteady attached flow.

4) Regime IV is an unsteady state with local nose separation. The topological description of the nose bubble is analogous to the one in regime II.

5) Regime V is the unsteady state with global separation. The separation bubble is described by a saddle of separation (global separation), a node of reattachment, two saddles $S_I$, and two nodes $N_I$, both symmetrically positioned with respect to the symmetry plane.

6) Regime VI is the unsteady state with global separation and "nose" vortices. The separation bubble is described by a saddle of separation (global separation), a node of reattachment, and two saddles $S_I$ and two foci $F$, both symmetrically positioned with respect to the symmetry plane. These foci are related to the origin of the nose vortices. When the two foci $F$ are identified among the surface critical points defining the separation bubble, the vortical pattern that is found in the nose area of the hemisphere-cylinder is called the nose vortex. Based on this definition, the three-dimensional topology pattern leads to distinguishing two subregimes into regime VI:

7) Regime VI.I is when the nose vortices do not emerge from the body surface. This is a previous step to the formation of the horn vortices: a transitional regime.

8) Regime VI.II is when the nose vortices emerge from the body surface. It is then when these nose vortices are called horn vortices.

The present phases diagram is representative for many configurations of the hemisphere-cylinder. The topology patterns found in regime VI are also found in the incompressible regime at moderate to high Reynolds numbers [14] and in the compressible regime at high Reynolds numbers [15].

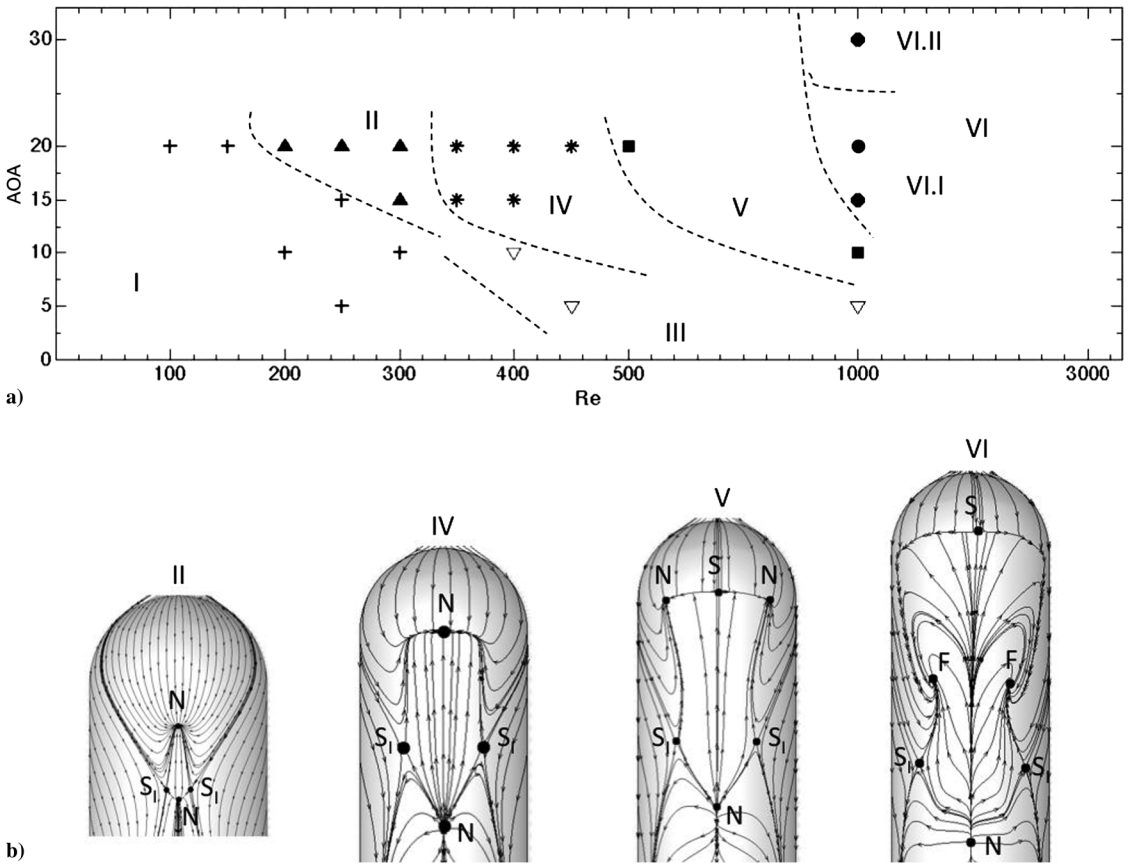


**Fig. 2 Representation of a) phase diagram as function of Reynolds number and AOA, and b) mean flow skin-friction lines and critical points in different Regimes.**

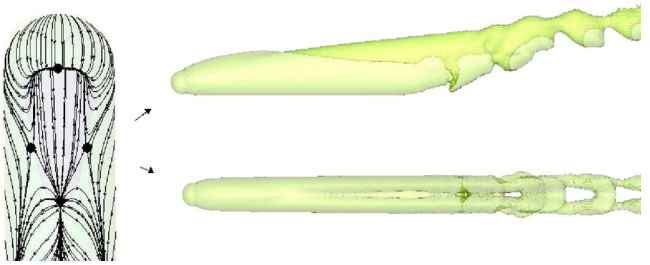

**Fig. 3 Instantaneous flow visualizations at $Re = 350$ and AOA = 20 deg (Regime IV): isosurface of streamwise velocity (right) and zoom-in of instantaneous skin-friction lines (left).**

Figure 2b shows the different surface topologies of the separation bubble of regimes II, IV, V, and VI. The onset of unsteadiness occurs incidentally in region IV, characterized by a local separation. However, at these conditions, the flow oscillations are related to a wake instability [34], and the flow around the separation bubble is mostly steady.

Finally, Fig. 3 shows isosurfaces of instantaneous streamwise velocity in a case contained in regime IV ($Re = 350$ and AOA = 20 deg). As can be seen, the flow is unsteady in the wake. The left part of the figure zooms in on the skin-friction lines obtained with instantaneous flow. As can be seen, both the instantaneous flow skin-friction lines shown in this figure and the mean flow skin-friction lines shown in Fig. 2b of regime IV are mostly identical.

## V. Flow Topology Patterns in the Hemisphere-Cylinder

The three topology patterns of the hemisphere-cylinder along the different regimes of the phase diagram are the leeward vortices, the separation bubble, and the horn vortices, which are found in the present numerical simulations. The same evolution of the flow regime under variations of Reynolds numbers and AOAs can be recovered following two different paths: maintaining the Reynolds number while varying the AOA, and maintaining the AOA while varying the Reynolds number. In the following, the evolution for increasing the Reynolds number is studied for a constant AOA by monitoring the location and classification of critical points, pressure gradients, and surface and volume streamlines.

### A. Formation of the Leeward Vortices

As a consequence of the AOA in the simulations performed over the HC, the crossflow pressure gradient effect causes the boundary layer to separate and roll up, leading to the origin of a pair of leeside vortices known as leeward vortices. It is possible to distinguish two different cases in the phase diagram, depending on the nature of the formation of the LV. On the one hand, if the origin of the vortices is not a critical point, the path of vortices formation is known as "open separation" (regime I). On the other hand, if the origin of the vortices is a critical point, the path of formation is known as "closed separation" (regime II) [14]. The following sections study in detail these two possible paths.

#### 1. *Leeward Vortices and Open Separation*

Figures 4a–4d show the evolution of the streamlines, skin-friction lines, and critical points at Reynolds number from 10 to 150 and AOA = 20 deg. At very low Reynolds numbers, the flow is fully attached and there is a single "limiting streamline" or "line of reattachment" on the surface of the body in the symmetry plane. This line acts as a barrier, dividing the body streamlines in two sides (symmetry plane).

Tobak and Peake [14] postulated that the initial configuration of critical points on the HC, when the flow is fully attached and with a zero AOA, are characterized by a node of attachment in the semisphere and a node of separation in the base of the body (cylinder base). When the Reynolds number increases, the node of separation is bifurcated into a new couple of points (node–saddle), leading to the configuration found in Figs. 4a–4b (bottom): node-saddle-node. The reattachment line ends in these critical points. As seen, the number of surface critical points over a three-dimensional body obeys the topological rules previously mentioned

$$\left(\sum N - \sum S = 2\right)$$

[4,42,43].

As the Reynolds number increases (Fig. 4b), the nodes from the cylinder base separate from each other. Crossflow pressure effects lead the skin-friction lines to converge into two new lines, the "lines of primary separation," which end in these two nodes. The two nodes prevent the "limiting" streamlines from crossing. This regime is characterized by an open separation, as the attachment lines are not anchored at a critical point.

Increasing the Reynolds number slightly (Fig. 4c), the two reattachment node points evolve into two foci. On the one hand, the focal points are always located in regions of maximum vorticity [5] and they can be considered as the origin of vortical formations. On the other hand, it is possible to identify two foci in the streamlines drawn in a plane transversal to the inflow velocity, close to the cylinder base (Fig. 4c top right): these two foci identify the LV. The formation of the LV remarks the influence of the crossflow pressure gradient over the entire geometry. Let us note that the origin of the LV is not reflected on the body surface by a critical point.

Finally, increasing the Reynolds number (Fig. 4d), two new couples of node–saddle points appear in the base of the HC as a result of two bifurcation processes.

#### 2. *Leeward Vortices and Closed Separation: Separation Bubble*

Figures 4d–4f show the transition from open to closed separation (from left to right). As the Reynolds number increases, the meridional pressure gradient (in the meridional or symmetry plane) causes the flow to separate at the nose of the body, which is manifested by the appearance of a node–saddle couple close to the region of minimum pressure at the nose. Increasing the Reynolds number, the concurrent effect of the meridional and crossflow pressure gradients around the nose region causes the separation saddle to bifurcate, giving rise to a new node–saddle couple. The critical points redistribute symmetrically to adopt the structurally stable configuration of Fig. 4f (top), conforming to the nose separation bubble. In this new topology, the separation lines associated with the leeward vortices are anchored to the two saddle points delimiting the nose separation bubble. Figure 4f (bottom) shows streamlines in a plane transversal to the HC, which is very close to these two saddle points. It is possible to see that the trajectory followed by the streamlines represents the origin of the leeward vortices.

Regarding the phases diagram of Fig. 2, it is possible to identify the origin of leeward vortices with open and closed separation in regimes I and II, respectively, in which the flow remains steady. As mentioned before, close separation in the leeward vortices is directly linked to the presence of a separation bubble. The topological bifurcations that are associated with flow separation are induced by crossflow and meridional pressure gradients (due to the three-dimensional nature of the geometry itself). These effects also contribute to the formation of the leeward vortices and the separation bubble. Furthermore, as expected, the separation and reattachment lines, which evidence the presence of the LV that interacts with the body, are always connected with the base of the HC, suggesting that the planar base of the cylinder may play an important role in the formation of the flow structures. [34]. This conclusion was also found in several investigations carried out in the literature [24,35,37].

#### 3. *Secondary Leeward Vortices*

The presence of the leeward vortices in the body surface is limited by the lines of primary separation and reattachment. However, by increasing the Reynolds number, the crossflow leads to a new couple of separation lines: the "secondary" separation lines. Crossflow

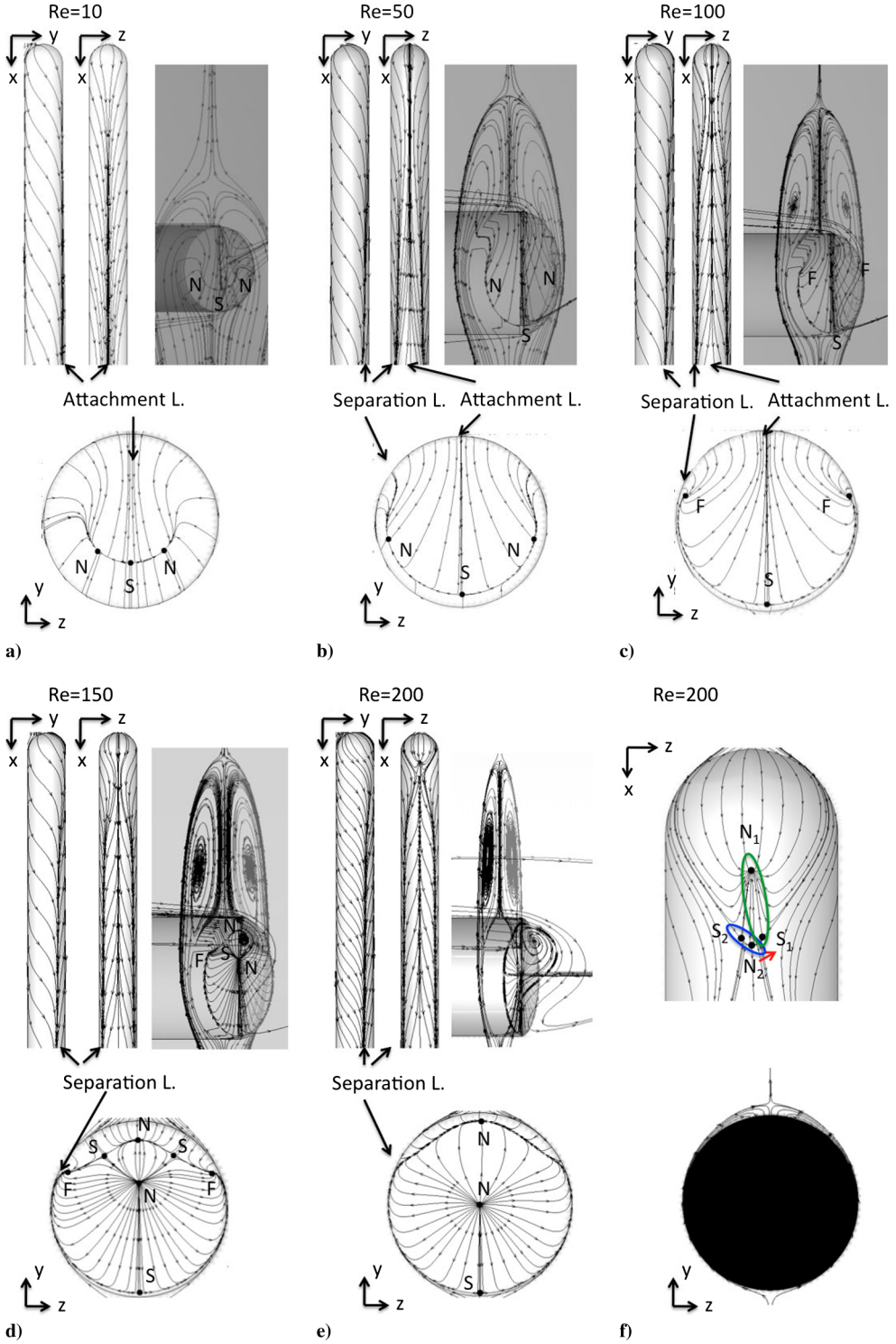


**Fig. 4 Critical points and skin-friction lines at AOA = 20 deg: a) $Re = 10$, b) $Re = 50$, c) $Re = 100$, d) $Re = 150$, and e–f) $Re = 200$. Figures 4a–4e show skin-friction lines, streamlines and critical points on the body (top left) and back surface (top right and bottom). Figure 4f shows the critical points, skin-friction lines (top) and streamlines (bottom) in a transversal plane $X/D = 1$ (L. is abbreviation of line).**

pressure gradient leads to the bifurcation of the reattachment lines. The topology presents a new couple of vortices between the body surface and the leeward vortices: the "secondary leeward" vortices. These secondary separation lines are only found in regime VI.

Figure 5 compares skin-friction lines and critical points in regime V (Fig. 5a) (leeward vortices) and regime VI (Fig. 5b) (primary and secondary leeward vortices). As seen, both skin-friction lines and critical points identify the presence of the primary and secondary leeward vortices. Skin-friction lines delimiting the primary leeward vortex have their upstream origin on two saddle points out of the symmetry plane. These saddle points delimit the recirculation region within the separation bubble. Finally, the line of flow separation corresponding to secondary leeward vortices emanates from a node in the plane of symmetry, and it has no connection to the nose separation bubble.

### B. Formation of the Separation Bubble

At $Re = 200$, the flow is separated (regime II). As shown in Fig. 4f, the separation bubble in this regime is defined by two nodes

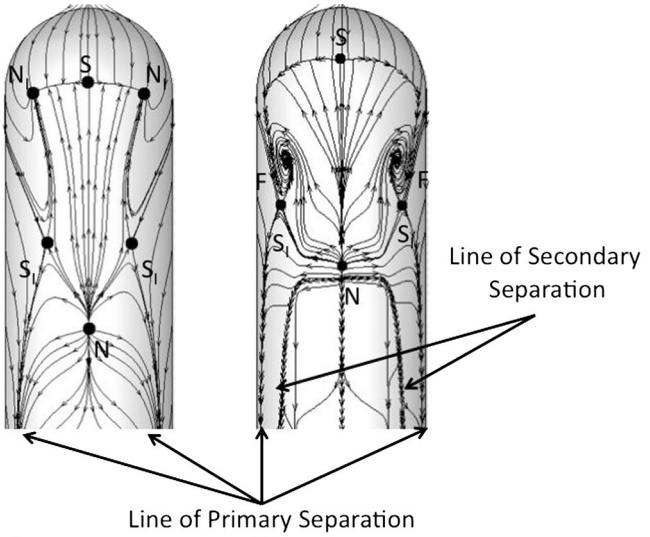


**Fig. 5 Critical points and mean flow skin-friction lines in a) regime V ($Re = 500$, AOA $= 20$ deg) and b) regime VI ($Re = 1000$, AOA $= 30$ deg).**

and two saddles. The point of separation is defined by the critical point found in the symmetry plane of the body, which corresponds to the region with the maximum adverse pressure gradient (detailed below). Thus, the points of the separation and reattachment are the two nodes, whereas the two saddles, as explained in previous sections, identify the origin of the LV.

The size of the separation bubble is measured as the distance from the point of separation to the point of reattachment in the symmetry plane. This size increases with the Reynolds number, and the set of critical points describing the bubble is qualitatively identical up to $Re = 450$. However, the flow becomes unsteady at $Re = 350$. The first linear global instability appears around $300 < Re \leq 350$ with a Hopf bifurcation that causes oscillations in the wake of the hemisphere-cylinder [34]. However, the three-dimensional separation bubble remains steady over this range of Reynolds number because the flow unsteadiness is concentrated in the wake. Figure 6 shows the critical points describing the separation bubble at $Re = 350$, 400, 500, and 1000 at AOA $= 20$ deg, which are conditions under which the flow is unsteady (regimes IV, V, and VI). At $Re = 500$, the increment of meridional pressure gradient causes the point of separation to branch off into a new couple of node–saddle points. The separation bubble is now described by two nodes $N_I$, two saddles $S_I$, a saddle of separation $S$, and a node of reattachment $N$. The separation lines of the primary LV are still emerging from the two saddles $S_I$.

Finally, the increased crossflow pressure gradient at $Re = 1000$ causes the two node points $N_I$ (found at $Re = 500$) to go through a local bifurcation and become foci $F$ (regime VI). The presence of a focal point is always linked to the presence of a saddle point and generates a vortex "sheet" [7]. These two foci delimit the extent of the horn vortices (see Sec. V.C for more details).

As seen, the topological patterns found by Tobak and Peake [7], who studied the flow around the same geometry at different AOAs and higher Reynolds number ($Re \simeq 10^5$, turbulent regime, incompressible flow), have been reproduced by the present results in regime VI. These flow structures were in good agreement with the ones presented by Bippes and Turk [15] in the same geometry at AOA $=$ 15 deg and $Re \simeq 2 \times 10^6$ in a compressible flow regime.

### 1. *Pressure Distribution*

An adverse pressure gradient (APG) occurs when the static pressure increases in the direction of the flowm causing a flow deceleration that, if strong enough, may lead to flow detachment and the formation of a nose separation bubble. This is the origin of flow separation and the separation bubble.

Pressure coefficients have been computed along the surface of the hemisphere-cylinder at Reynolds numbers ranging from 100 to 1000 (AOA $= 20$ deg) to study more in depth the origin and evolution of the separation bubble. The results obtained have been compared with the equivalent potential flow (obtained with the same numerical solver) for which separation cannot occur, with the aim of highlighting the relation between the pressure gradients and the topology of skin-friction lines.

The pressure coefficient is defined as

$$C_p = \frac{p - p_\infty}{(1/2)\rho_\infty U_\infty^2} \tag{3}$$

where $p$ and $p_\infty$ are local and far-field pressures, respectively; $\rho_\infty$ is the density; and $U_\infty$ is the far-field velocity.

It is known that the origin of the separation bubble starts when the APG surpasses a certain value [44], and it is reflected in the variations of $C_p$. In the meridional plane (symmetry), this coefficient decreases to negative values (which means that the local pressure is smaller than far field) with $C_{\text{peak}}$ as a minimum value, and subsequently increases slowly. In this growth, it is possible to identify a zone in which $C_p$ remains nearly constant: this is the "plateau" region and it describes the SB. The points of separation and reattachment are located upstream and downstream of this zone, respectively.

Figure 7 shows the pressure coefficient in $\Phi = 0$ deg for Reynolds numbers ranging from 100 to 1000 and compared with potential flow theory. The point $X/D = 0$ corresponds to the

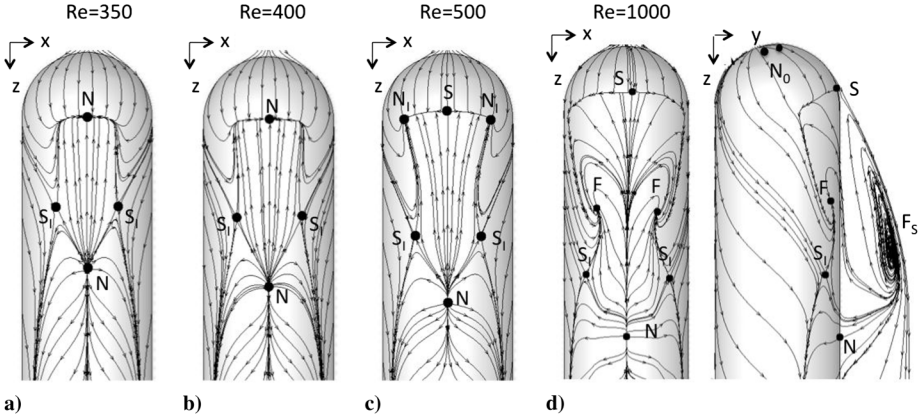


**Fig. 6 Critical points and mean flow skin-friction lines at AOA $= 20$ deg and a) $Re = 350$, b) $Re = 400$, c) $Re = 500$, and d) $Re = 1000$.**

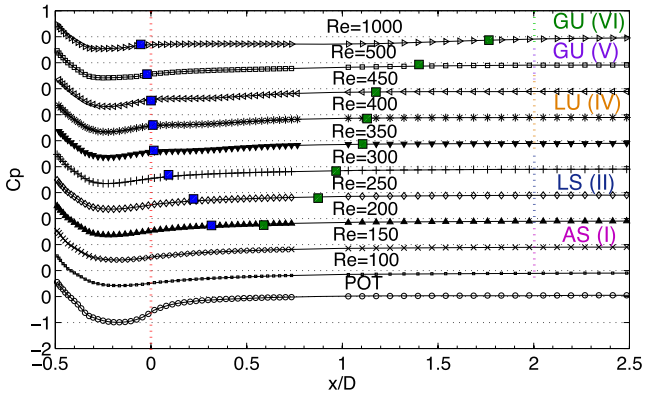


**Fig. 7 Pressure coefficient distribution along $X/D$ (with $Y = Z = 0$) at AOA = 20 deg, $100 < Re < 1000$, and $\Phi = 0$ deg, compared with potential flow theory (POT).**

junction point between the hemisphere and the cylinder. The region of $C_{peak}$ and the region of constant $C_p$ are identified. $C_{peak}$ is found in the area with $X/D < 0$. However, the position of $C_{peak}$ is farther from $X/D = 0$ in the viscous calculations than in the calculations done using potential flow theory. As expected, the results obtained with potential flow theory differ from the calculations obtained with viscous theory. The figure also details the critical points in the nose of the HC in regimes I (AS denotes attached, steady), II (LS denotes local separation, steady), IV (LU denotes local separation, unsteady), V (GU denotes global separation, unsteady), and VI (GU denotes global separation, unsteady). The points of separation and reattachment are marked by squares.

As seen, if the AOA is maintained, the size of the separation bubble increases when the Reynolds number increases. In addition, it is observed that, in the particular cases shown in the figure, the point of separation moves from $X/D > 0$ (steady regimes) to $X/D < 0$ (unsteady regimes, global separation). Finally, the point of reattachment moves upstream as the Reynolds number increases.

### C. Formation of the Horn Vortices

The main goal of this section is to detail the path of formation of the horn vortices. The origin of these vortices lies in the two foci $F$ found in the nose of the body surface defining the three-dimensional separation bubble [12,14]. As previously seen, these two foci are conforming the bubble in the cases contained in regime VI. The evolution from regime V to regime VI (formation of HV) is studied in detail in Fig. 8. In regime V, the separation bubble remains steady, but it is unsteady in regime VI. The top of Fig. 8 shows the contours of the $C_p$ coefficient and the critical points on the body surface that bounds the SB. The middle part of the figure shows the evolution of the focus $F_s$ in the symmetry plane. The distance from this focus to the body surface ($Y/D = 0$) measures the height of the SB. Table 2 shows the position of the critical points and the position of the focus $F_s$ found in the symmetry plane of the SB.

Finally, Fig. 8 (bottom) shows the evolution from $N_I$ to $F$ of the critical points describing the SB. Their corresponding eigenvalues have been represented in the $QR$ chart [41]. The node (stable) is transformed into a focus (stable) when the eigenvalue cross the line marked with "T." In the figure, cases 1 and 2 show two events contained in regime V ($Re = 500$, AOA $= 20$ deg and $Re = 1000$, AOA $= 10$ deg, respectively). The size of the bubble is smaller in case 1. This suggests that, regardless the Reynolds number, the size of the SB decreases when the AOA increases. The same effect is found in cases 3 and 4, shown in the same figure, that compares two events

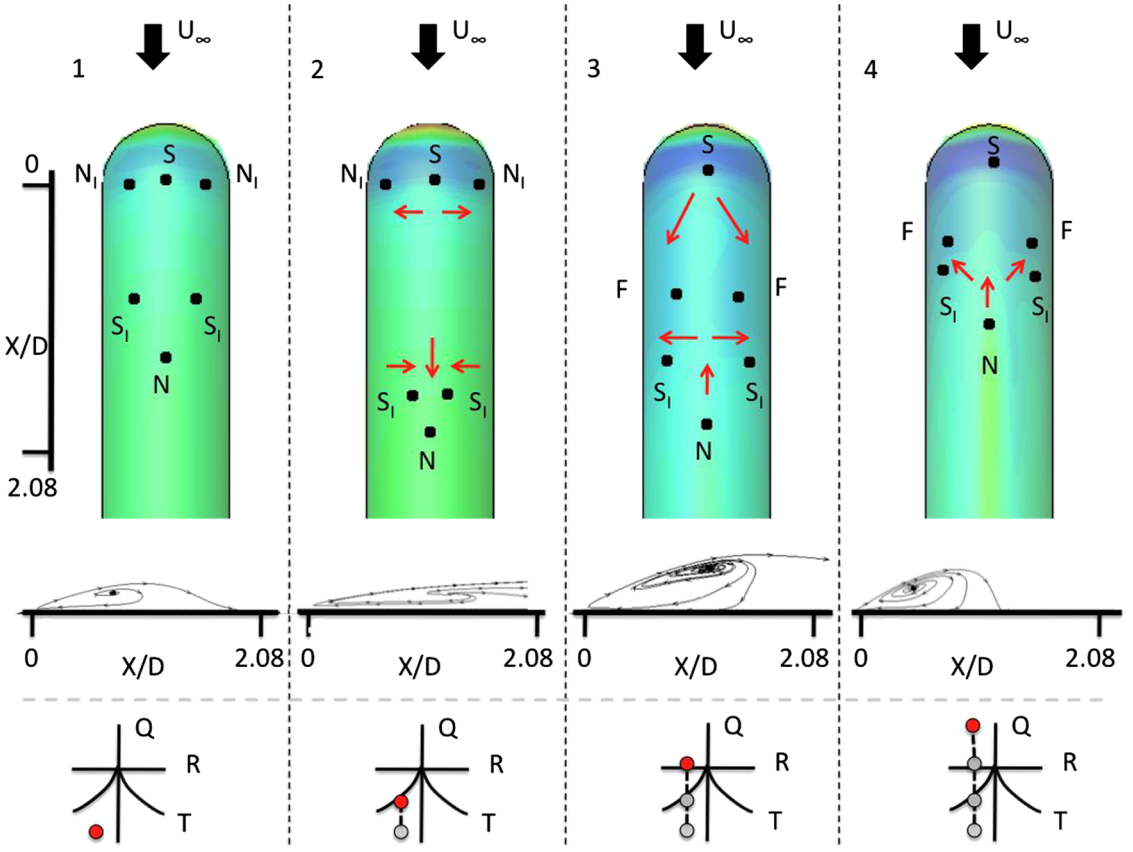


**Fig. 8 Global separation. Sketch showing the evolution of the critical points defining the SB (correspondence with Table 2). Surface critical points and $C_p$ (top), the arrows represent free stream velocity. Focus $F_c$ in the symmetry plane of the SB (middle). Eigenvalues in the $QR$ chart [41] (bottom).**

**Table 2 Critical points describing the nose separation bubble[a]**

| | $(X/D, \Phi)$ | | | | $(X/D, Y/D)$ |
|---|---|---|---|---|---|
| Case | Separation | Attachment | Sides | Extra | Symmetry |
| $Re = 500$ | $S$ | $N$ | $S_I$ | $N_I$ | $F_S$ |
| AOA $= 20$ deg | (−0.056, 0) | (1.36, 0) | (0.96, ±28.6) | (0, ±39.8) | (0.8, 0.18) |
| $Re = 1000$ | $S$ | $N$ | $S_I$ | $N_I$ | $F_S$ |
| AOA $= 10$ deg | (−0.020, 0) | (1.92, 0) | (1.6, ±15.6) | (0, 50.1) | (1.44, 0.14) |
| $Re = 1000$ | $S$ | $N$ | $S_I$ | $F$ | $F_S$ |
| AOA $= 20$ deg | (−0.08, 0) | (1.84, 0) | (1.36, ±41.6) | (0.8, ±28.6) | (1.12, 0.61) |
| $Re = 1000$ | $S$ | $N$ | $S_I$ | $F$ | $F_S$ |
| AOA $= 30$ deg | (−0.16, 0) | (1.12, 0) | (0.72, ±48.4) | (0.4, ±41.6) | (0.36, 0.18) |

[a]$S$ = saddle, $N$ = node, $F$ = foci, $\Phi$ = azimuthal angle measured clockwise, $X/D$ and $Y/D$ correspond to streamwise and wall-normal component, respectively, non-dimensionalized with the diameter of the hemisphere-cylinder $D$.



from regime VI ($Re = 1000$, AOA $= 20$ deg and $Re = 1000$, AOA $= 30$ deg, respectively).

Coming back to the evolution of the critical points in the SB from regime V to VI (from left to right in Fig. 8), case 1 is established as the baseline state (critical points and $C_p$ coefficient) in the forthcoming explanation. As seen in case 2, increasing the Reynolds number (or AOA) results in the meridional pressure gradient increasing and, as a consequence, the length of the SB also increases. This effect and also the crossflow pressure gradient produce the two saddles $S_I$ to approximate each other. The height of the SB has also diminished. Increasing the Reynolds number slightly more, the combined effect of both the crossflow and meridional pressure gradients induces a crossflow and longitudinal deceleration (respectively) and leads to the transformation of the two nodes $N_I$ into the two foci $F$. This effect is evidenced in case 3. As mentioned before, the focal points are always located in regions of maximum vorticity. Hence, these two foci suggest a vorticity rise inside the SB. At the same time, the results also show a notable growth in the height of the SB. Finally, increasing the Reynolds number slightly more, meridional and crossflow pressure gradients lead to an increase in the foci $F_I$ intensity (in the $QR$ chart, $Q$, which is discriminant of the Jacobian matrix defined in Sec. III, is more positive), and consequently it is expected that the vorticity within the SB also increases. This effect is evidenced in case 4, where the results also show that the length and height of the bubble are diminished. At this point, the intensity of these foci is sufficiently high to become the origin of the HV. However, surface topology is not sufficient to address this hypothesis, and using the three-dimensional flow topology is necessary.

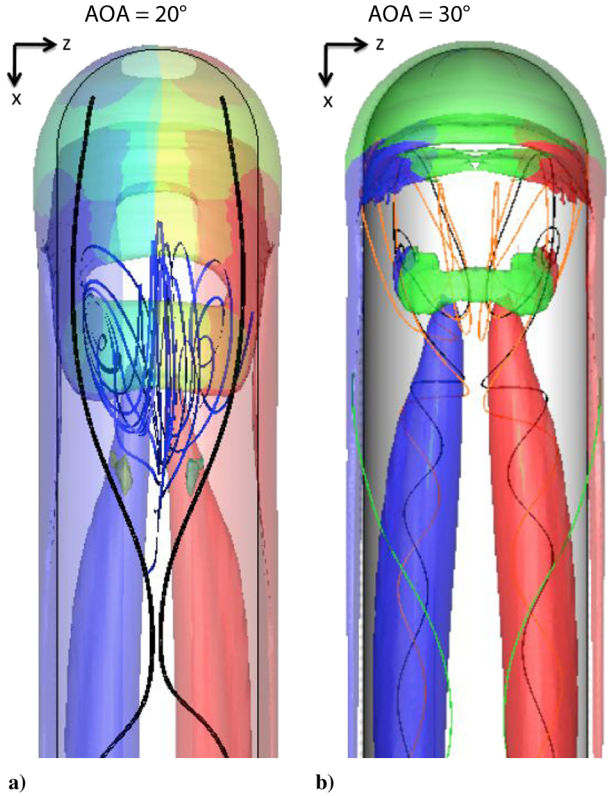


**Fig. 9 Three-dimensional flow topology at $Re = 1000$. Mean flow volume streamlines and isosurfaces of instantaneous $Q$ colored with spanwise vorticity (red and blue colors represent the counter-rotating vortices, and green color shows the zero vorticity regions). a) AOA $= 20$ deg, $Q = 1300$; and b) AOA $= 30$ deg, $Q = 4000$.**

### 1. *Three-Dimensional Flow Topology and Skin-Friction Lines*

A three-dimensional representation of the skin-friction lines of the HC has been performed. To this aim, the volume streamlines have been computed around the bubble nose of the body at two different flow conditions from regime VI ($Re = 1000$ and AOA $= 20$ and 30 deg). The flow was unsteady around the nose of the HC; thus, the streamlines computed corresponded to the mean flow. Figure 9 shows the coherent structures detected with $Q$ criterion [43], displaying the vorticity and a rake of volume streamlines. As seen, it is possible to distinguish the SB and a pair of counter-rotating vortices (the nose vortices, classified in region VI of the phases diagram in Fig. 2). Volume streamlines reveal that, at an AOA of 30 deg, these vortices emerge from the body surface; thus, they are called HVs. Under these conditions, the intensity of the streamwise vorticity is stronger than at AOA $= 20$ deg. This result is in good agreement with the description of Fig. 8. As seen in the diagram, at AOA $= 20$ deg (case 3), when the intensity of the surface foci is not strong enough, crossflow separation is still the origin of the vortices found in the hemisphere-cylinder. These vortices can be considered as leeward vortices; however, since the two foci $F$ from which they emerge are present in the description of the nose separation bubble, these vortices are renamed as nose vortices. The terminology presented in this paper considers these vortices as a transition that will evolve into the HV.

Figure 10 shows the same vortical structures detected with $Q$ and some selected volume streamlines, emerging from the two foci $F$. The trajectory followed by these streamlines and their interaction with the vortices pattern represented by isosurfaces of $Q$ criterion show that, at AOA $= 20$ deg, the surface foci $F$ (stable, sink of skin-friction lines) are connected to the focus $F_s$ at the symmetry plane (unstable, source of skin-friction lines). However, at AOA $=$ 30 deg, the nose vortices emerge from those foci $F$; thus, they are referred to as HVs. Finally, it is worth mentioning that the crossflow pressure gradient, considered as the main contributor to the origin of the LV, is also interacting with the HV downstream of the SB (see the rake of volume streamlines in Fig. 9b and the volume streamline in Fig. 10b).

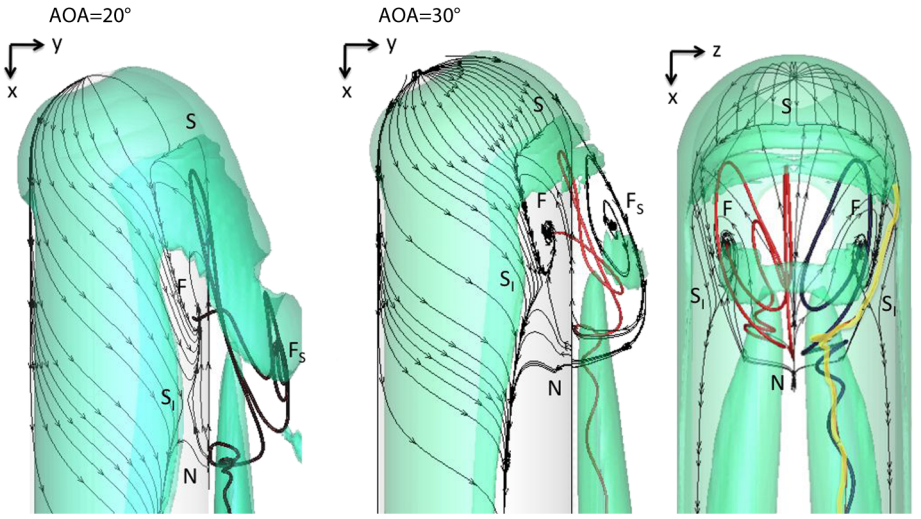


a) b)

**Fig. 10 Three-dimensional flow topology at $Re = 1000$. Mean flow volume streamlines and isosurfaces of instantaneous $Q$: a) AOA = 20 deg, $Q = 1300$; and b) AOA = 30 deg, $Q = 4000$.**

## VI. Conclusions

The hemisphere-cylinder at a high AOA is a geometry representative of submarine bodies, aircraft fuselages, and torpedoes or missiles (i.e., Infra Red Imaging System Tail (IRIS-T), AIM-132, . . . ); these applications operate at high Reynolds numbers and, in some cases, in transonic/supersonic regimes.

The study performed in this paper addressed the three-dimensional separated flow topologies that developed as the AOA was increased. The findings of the study at incompressible and low-Reynolds-number flow conditions shed light on the physical phenomena occurring at higher Reynolds number. Concerning the topology of the three-dimensional separated flow, it was noted by Bippes and Turk [15] and Peake and Tobak [1] that the flow patterns encountered on the hemisphere-cylinder at very high Reynolds numbers and transonic conditions were qualitatively identical to the ones found for low Reynolds numbers in incompressible flow.

Three different flow structures surround the hemisphere-cylinder under separated flow conditions; i.e., separation bubbles, horn vortices, and leeward vortices. With the aim of studying the origin and evolution of the complex flow patterns, this paper presents three-dimensional numerical simulations for a variety of Reynolds numbers and AOAs.

Critical point theory has been applied to the simulated flowfields to provide, for the first time for this geometry, a bifurcation diagram that classified the different flow topology regimes as a function of the Reynolds number and the AOA. Six different flow regimes have been distinguished and studied in detail. Along the six studied regimes, it was shown that the separation bubble appeared initially defined as a local separation phenomenon (node of separation) and evolved to global separation (saddle of separation) when the flow conditions changed (Reynolds number or AOA increase). Furthermore, the two foci found in the critical points that defined the separation bubble were a result of a high-vorticity region that contributed to modify the size of the bubble and evidenced the presence of the HV. Finally, it was found that the leeward vortices, generated by the crossflow pressure gradient, were the most robust characteristic pattern of this geometry, found in both steady and unsteady flows and regardless of the presence of nose separation, except for very low Reynolds numbers and AOAs.

The deeper understanding gained regarding the topologies of the three-dimensional separated flow can be useful in the future to improve existing industrial methods for the calculation of aerodynamic forces and moments. These methods typically rely on potential flow calculations that fail to a large extent when massive separation exists. Currently existing methods for introducing the effect of flow separation in engineering design tools are devised for two-dimensional separation, and their extension to three-dimensional flows is precluded by the absence of a clear description of the substantially more complex three-dimensional separation. In addition, understanding the manner in which flow separation occurs in three-dimensional geometries can help to devise flow control strategies that improve the aerodynamic performance and capabilities of this class of aerodynamic bodies.

## Acknowledgments

Support from the Spanish Ministry of Science and Innovation through grant TRA2012-34148 "Mejoras del Rendimiento Aerodinámico de alas Mediante Control de Mecanismos de Inestabilidad Global" is gratefully acknowledged. Support from Marie Curie grant PIRSES-GA-2009-247651 "FP7-PEOPLE-IRSES: ICOMASEF–Instability and Control of Massively Separated Flows" is gratefully acknowledged. Support of European project Fly High 518156-LLP-1-2011-1-ATCOMENIUS-CMP is gratefully acknowledged. D. Rodríguez acknowledges funding from the "Science Without Borders" program from Coordenação de Aperfeiçõamento de Pessoal de Nível Superior (CAPES), Brazil. This work was supported by the Multi-Modal Australian Sciences Imaging and Visualisation Environment. Discussions with M. Chong are kindly acknowledged.

## References

[1] Peake, D., and Tobak, M., "Three-Dimensional Interaction and Vortical Flows with Emphasis on High Speeds," Fluid Dynamics Panel of AGARD, Rept. AGARD-AG-252, 1980.

[2] Hoang, N., Rediniotis, O., and Telionis, D., "Symmetric and Asymmetric Separation Patterns over a Hemisphere-Cylinder at Low Reynolds Number and High Incidences," *Journal of Fluids and Structures*, Vol. 11, No. 7, 1997, pp. 793–817. doi:10.1006/jfls.1997.0106

[3] Legendre, R., "Séparation de L'écoulement Laminaire Tridimensional," *La Recherche Aéronautique*, Vol. 54, Nov.–Dec. 1956, pp. 3–8.

[4] Lighthill, M., "Attachment and Separation in Three-Dimensional Flow," edited by Rosenhead, L., *Laminar Boundary Layers*, Dover Publ., New York, 1963, pp. 72–76.

[5] Perry, A. E., and Fairlie, B. D., "Critical Points in Flow Patterns," *Advances in Geophysics*, Vol. 18B, 1974, pp. 299–315.

[6] Dallmann, U., "Topological Structures of Three-Dimensional Vortex Flow Separations," *16th Fluid and Plasmadynamics Conference*, DFVLR-IB 221-82 A07, Danvers, MA, 1982.

[7] Tobak, M., and Peake, D., "Topoogy of Two-Dimensional and Three-Dimensional Separated Flows," AIAA Paper 1979-1480, 1979.

[8] Perry, A., and Chong, M., "A Description of Eddying Motions and Flow Patterns Using Critical-Point Concepts," *Annual Review of Fluid Mechanics*, Vol. 19, No. 1, 1987, pp. 125–155. doi:10.1146/annurev.fl.19.010187.001013

[9] Hsieh, T., "An Investigation of Separated Flow About a Hemisphere-Cylinder at 0 to 19 deg Incidence in the Mach Number Range from 0.6 to 1.5," Propulsion Wind Tunnel Facility Arnold Engineering Development Center Air Force Systems Command Arnold Air Force Station, TN, Nov. 1976.

[10] Hsieh, T., "Hemisphere-Cylinder in Low Supersonic Flow," *AIAA Journal*, Vol. 13, No. 12, 1975, pp. 1551–1552. doi:10.2514/3.60579

[11] Hsieh, T., "An Investigation of Separated Flow About a Hemisphere-Cylinder at Incidence in the Mach Number Range from 0.6 to 1.5," AIAA Paper 1977-0179, 1977.

[12] Fairlie, B., "Flow Separation on Bodies of Revolution at Incidence," *7th Australian Hydraulics and Fluid Mechanics Conference*, Brisbane, Australia, Aug. 1980.

[13] Peake, D., and Tobak, M., "Three-Dimensional Flows About Simple Components at Angle of Attack," NASA TM 84226, 1980.

[14] Tobak, M., and Peake, D., "Topology of Two-Dimensional Separated Flows," *Annual Review of Fluid Mechanics*, Vol. 14, No. 1, 1992, pp. 61–85. doi:10.1146/annurev.fl.14.010182.000425

[15] Bippes, H., and Turk, M., "Oil Flow Patterns of Separated Flow on a Hemisphere-Cylinder at Incidence," Rept. DFVLR-FB 84-20, 1984.

[16] Meier, H., and Kreplin, H., "Experimental Investigations of the Boundary Layer Transition and Separation on a Body of Revolution," *Zeitschrift für Flugwissenschaften und Weltraumforschung*, Vol. 4, March–April 1980, pp. 65–71.

[17] Kreplin, H., Vollmers, H., and Meier, H., "Measurements of the Wall Shear Stress on an Inclined Prolate Spheroid," *Zeitschrift für Flugwissenschaften und Weltraumforschung*, Vol. 6, 1982, pp. 248–252.

[18] Costis, C. E., and Telionis, D. P., "Unsteady Vortical Wakes over a Prolate Spheroid," AIAA Paper 1984-0419, 1984.

[19] Costis, C. E., Hoang, N. T., and Telionis, D. P., "Laminar Separating Flow over a Prolate Spheroid," *Journal of Aircraft*, Vol. 26, No. 9, 1989, pp. 810–816. doi:10.2514/3.45845

[20] Hsieh, T., and Wang, K., "Three-Dimensional Separated Flow Structure over a Hemisphere-Cylinder," *Journal of Fluid Mechanics*, Vol. 324, 1996, pp. 83–108. doi:10.1017/S0022112096007847

[21] Meade, A., and Schiff, L., "Experimental Study of Three-Dimensional Separated Flow Surrounding a Hemisphere-Cylinder at Incidence," AIAA Paper 1987-2492, 1987.

[22] Ying, S. X., Schiff, L. B., and Steger, J. L., "A Numerical Study of Three-Dimensional Separated Flow Past a Hemisphere-Cylinder," AIAA Paper 1987-1207, 1987.

[23] Hoang, N., Redinioti, O., and Telionis, D., "Hemisphere-Cylinder at Incidence at Intermediate to High Reynolds Numbers," *AIAA Journal*, Vol. 37, No. 10, 1999, pp. 1240–1250. doi:10.2514/2.592

[24] Gross, A., Jagadeesh, C., and Fasel, H., "Numerical Investigation of Three-Dimensional Separation on Axisymmetric Bodies at Angle of Attack," AIAA Paper 2012-0098, 2012.

[25] Rodriguez, D., "Global Instability of Laminar Separation Bubbles," Ph. D. Dissertation, Univ. Politécnica de Madrid, School of Aeronautics, Madrid, 2010.

[26] Crow, S. C., and Champagne, F. H., "Orderly Structure in Jet Turbulence," *Journal of Fluid Mechanics*, Vol. 48, No. 3, 1971, pp. 547–591. doi:10.1017/S0022112071001745

[27] Gaster, M., Kit, E., and Wygnasky, I., "Large-Scale Structures in a Forced Turbulent Mixing Layer," *Journal of Fluid Mechanics*, Vol. 150, 1985, pp. 23–39. doi:10.1017/S0022112085000027

[28] Reynolds, W. C., and Hussain, A. K. M. F., "The Mechanics of an Organized Wave in Turbulent Shear Flow, Part 3: Theoretical Models and Comparisons with Experiments," *Journal of Fluid Mechanics*, Vol. 54, No. 2, 1972, pp. 263–288. doi:10.1017/S0022112072000679

[29] Bohorquez, P., Sanmiguel-Rojas, E., Sevilla, A., Jimenez-Gonzalez, J., and Martinez-Bazan, C., "Stability and Dynamics of the Laminar Wake Past a Slender Blunt-Based Axisymmetric Body," *Journal of Fluid Mechanics*, Vol. 676, 2011, pp. 110–144. doi:10.1017/jfm.2011.35

[30] Sanmiguel-Rojas, E., Martínez-Bazán, C., and Chomaz, J. M., "Global Mode Analysis of Axisymmetric Bluff-Body Wakes: Stabilization by Base Bleed," *Physics of Fluids*, Vol. 21, No. 11, 2009, Paper 114102. doi:10.1063/1.3259357

[31] Tomboulides, A. G., and Orszag, S. A., "Numerical Investigation of Transitional and Weak Turbulent Flow Past a Sphere," *Journal of Fluid Mechanics*, Vol. 416, 2000, pp. 45–73. doi:10.1017/S0022112000008880

[32] Schewe, G., "Reynolds-Number Effects in Flow Around More-or-Less Bluff Bodies," *Journal of Wind Engineering*, Vol. 89, 2001, pp. 1267–1289.

[33] Haragus, M., and Iooss, G., *Local Bifurcations, Center Manifolds, and Normal Forms in Infinite Dimensional Dynamical Systems*, Springer–Verlag, Berlin, 2010.

[34] Le Clainche, S., Rodriguez, D., Theofilis, V., and Soria, J., "Flow Around a Hemisphere-Cylinder at High Angle of Attack and Low Reynolds Number. Part II: POD and DMD Applied to Reduced Domains," *Aerospace Science and Technology*, Vol. 44, 2015, pp. 88–100. doi:10.1016/j.ast.2014.10.009

[35] Le Clainche, S., "Instability and Topology Bifurcations on a Hemisphere-Cylinder at High Angle of Attack," Ph.D. Dissertation, Univ. Politécnica de Madrid, School of Aeronautics, Madrid, 2013.

[36] Bohorquez, P., and Parras, L., "Three-Dimensional Numerical Simulation of the Wake Flow of an Afterbody at Subsonic Speeds," *Theoretical and Computational Fluid Dynamics*, Vol. 27, No. 1, 2013, pp. 201–218. doi:10.1007/s00162-011-0251-9

[37] Sanmiguel-Rojas, E., Jiménez-González, J. I., Bohorquez, P., Pawlak, G., and Martínez-Bazán, C., "Effect of Base Cavities on the Stability of the Wake Behind Slender Bluntbased Axisymmetric Bodies," *Physics of Fluids*, Vol. 23, No. 11, 2011, Paper 114103. doi:10.1063/1.3658774

[38] Rancic, M., Purser, J., and Mesinger, F., "A Global-Shallow Water Model Using an Expanded Spherical Cube," *Quarterly Journal of the Royal Meteorological Society*, Vol. 122, No. 532, 1996, pp. 959–982. doi:10.1002/(ISSN)1477-870X

[39] Le Clainche, S., Li, J. I., Theofilis, V., and Soria, J., "Flow Around a Hemisphere-Cylinder at High Angle of Attack and Low Reynolds Number. Part I: Experimental and Numerical Investigation," *Aerospace Science and Technology*, Vol. 44, 2015, pp. 77–87. doi:10.1016/j.ast.2014.03.017

[40] Le Clainche, S., Gomez, F., Li, J. I., Theofilis, V., and Soria, J., "Structural Analysis on a Hemisphere-Cylinder at Moderate Reynolds Number and High Angle of Attack," AIAA Paper 2013-0387, 2013.

[41] Chong, M., Soria, J., Perry, E., Chacing, J., Na, I., and Cantwell, B. J., "Turbulence Structures of Wall-Bounded Shear Flows Found Using DNS Data," *Journal of Fluid Mechanics*, Vol. 357, 1998, pp. 225–247. doi:10.1017/S0022112097008057

[42] Davey, A., "Boundary-Layer Flow at a Saddle Point of Attachment," *Journal of Fluid Mechanics*, Vol. 10, No. 4, 1961, pp. 593–610. doi:10.1017/S0022112061000391

[43] Hunt, J., Wray, A., and Moin, P., "Eddies, Stream, and Convergence Zones in Turbulent Flows," Center for Turbulence Research Rept. CTR-S88, 1988, p. 193.

[44] Schlichting, H., *Boundary Layer Theory*, 7th ed., McGraw–Hill, New York, 1979.


B. Ganapathisubramani
*Associate Editor*